



The origin of the two-plateaued or one-plateaued open circuit voltage in Li-S batteries

Yuxiao Lin^{a,1}, Jing Zheng^{b,1}, Chunsheng Wang^{b,**}, Yue Qi^{a,*}

^a Department of Chemical Engineering and Materials Science, Michigan State University, East Lansing, MI, 48824, USA

^b Department of Chemical and Biomolecular Engineering, University of Maryland, College Park, MD, 20742, USA

ARTICLE INFO

Keywords:

Li-S batteries
First principle calculation
Li-polysulfide solvation
Nano structure design
Concentrated electrolyte

ABSTRACT

Li-S batteries have been actively pursued as a storage device of high energy density. Interestingly, most of the discharging curves for Li-S batteries show either one plateau or two plateaus. Understanding the mechanism and conditions of the one-plateaued discharging curves can provide guidance for Li-S battery design to prevent the Li-polysulfide (Li-PS) dissolution. In this article, we first calculated a solvent-dependent open circuit voltage (OCV) using density functional theory (DFT) when both crystals (S, Li₂S, Li) and dissolved Li-PS molecules (such as Li₂S₄) are involved in the discharging reactions. We successfully predicted the two-plateaued OCV with fully solvated Li-PS and the one-plateaued OCV with non-solvated Li-PS, in agreement with experimental observations. Furthermore, if Li-PS changes from partial or non-solvated state to fully solvated state, its formation energy increases, leading to a transition from the one-plateaued to the two-plateaued OCV. The partially solvated Li-PS can be realized either by a highly-concentrated electrolyte or by minimizing the pore size in the carbon/sulfur composites to limit the number of solvents transported into the pores, which changes the complex liquid-solid reactions of Li-S chemistry to a single solid-state reaction. The solid-state reaction allows Li-S batteries to operate in lean electrolytes with less Li excess. A new Li-PS dissolution mitigation strategy based on this synergistic effect is therefore proposed by modeling and verified by experiments.

1. Introduction

Li-S batteries have been actively pursued as one of the next generation energy storage devices because of their high specific capacity, high specific energy density, and low cost [1,2]. The potential curve of Li-S batteries is a direct signature of the electrochemical reactions occurring during charge/discharge of sulfur cathodes. Interestingly, most of the discharging curves for sulfur cathode show either a single plateau or two plateaus. The two-plateaued discharging curves of sulfur cathode were typically observed in ether-based liquid electrolytes [3–6]. The first plateau at 2.3–2.4 V has been attributed to the lithiation reaction from elemental S to dissolved Li-polysulfide (Li-PS). The second plateau at around 2.0–2.1 V has been attributed to the continuous lithiation of the dissolved Li-PS to the precipitated crystalline Li₂S₂ and Li₂S. In comparison, the one-plateaued discharging curves, sometimes with a slope, were believed to be the characteristic for the solid-state reaction from solid state S to solid-state Li₂S₂ and Li₂S, when the soluble Li-PS was not

formed due to the absence of free solvent in electrolytes [7–9]. The sloped plateau was due to the overpotential in solid electrolyte [10]. Sulfur cathodes in which S was confined in the nanopores of a carbon matrix displayed one-plateaued discharging curves in carbonate-based liquid electrolytes because S was sealed inside of carbon pores by in-situ formed solid electrolyte interphase (SEI) [11–14]. So far, there is no consistent model that has clarified the difference between the two-plateaued and one-plateaued OCVs from the reaction mechanisms point of view.

Li-S batteries suffer from Li-PS shuttling in the liquid reaction at the high-voltage plateau and poor reaction kinetics in the solid-state reaction low-voltage plateau. Therefore the Li-S batteries are very challenged to operate in the lean electrolyte with less Li excess in the anode [15]. In addition, even though solid electrolytes can mitigate Li-PS shuttling problem, the induced high overpotential and slow Li transport still limited the practical energy and power density [16]. Alternatively, nanopore-C/S cathode materials in the carbonate-based liquid

* Corresponding author.

** Corresponding author.

E-mail addresses: cswang@umd.edu (C. Wang), yueqi@egr.msu.edu (Y. Qi).

¹ These authors contributed equally to this work.

electrolyte with only one-plateau demonstrated supper cycling stability due to the absence of Li-PS and fast Li transport in the liquid electrolyte, [13,14,17–22]. Both confinement and separation mechanisms had been proposed to explain this unique phenomenon. In the confinement mechanism, it was hypothesized that the pore volume was too small to store S₈ monomer and long chain Li-PS [23,24]. Thus, the small S allotropes such as S₂ and S₄ were incorporated into the pores and long chain Li-PS such as Li₂S₈, Li₂S₆, and Li₂S₄ could not be generated in the discharging reaction due to the confinement of nanopores. In the separation mechanism, the formation of SEI from the decomposition of carbonate electrolytes could seal the pore, blocking the electrolytes from diffusing into the pores [20]. In ether electrolytes with less SEI formation, if the pore size was well controlled to only allow Li-ion diffusion while blocking both Li-PS and electrolyte solvent, there would be a great chance to trap the Li-PS inside the pores [20,25]. The plateaus on the discharging curves were also related to the chemistry of electrolyte solvent [26]. A single plateau was observed when electrolyte solvent with low Li-PS solubility was used, while two plateaus were observed with an electrolyte that could dissolve more Li-PS [27]. The one-plateaued discharging curves and mitigated Li-PS shuttle problem were also observed with extremely high Li salt concentration in the electrolyte [28–32]. Therefore, the discharge plateau is highly dependent on the solvation status of the Li-PS, which is subject to change with the pore size, solvent chemistry, and electrolyte concentration. Besides, single metal atoms were reported to trap the dissolved Li-PS, catalytically convert the discharge reaction [33], but no obvious change of discharge plateaus was observed.

These fundamentals must be understood in order to precisely design Li-S batteries, as neither of the design idea discussed above provided a complete solution for Li-S batteries. In terms of the pore size, the optimum pore size only allowing Li-ion diffusion, according to our recent investigation, was less than 1 nm, which requires costly synthesis processes [23,24,34]. If the pore size is within 3–5 nm, larger than the solvent molecule and soluble Li-PS, a carbonate electrolyte [17,35–37] has to be used to seal the pores through SEI formation. Unfortunately, Li metal anode does not cycle well in carbonate based electrolyte [38–40]. Furthermore, the use of the highly-concentrated electrolyte suffers from high viscosity and slow Li transport property [41,42]. Thus, new Li-S design strategies, that simultaneously tuning the pore size, solvent chemistry, and electrolyte concentration, are required.

Theoretical prediction of the solvent dependent open circuit potential (OCV) still faces challenges. Density functional theory (DFT) has long been used to predict the OCV of electrodes that store lithium via intercalation [43,44] and alloying [45,46] solid-state reactions. In fact, if the lithiation reaction of S was modeled as a solid-state reaction, Li₂S would be the only thermodynamically stable phase, consistent with the Li-S phase diagram [47]. Using crystalline S and Li₂S, Yang et al. computed the convex hull of all crystalline Li-PS (without solvation due to periodic boundary conditions) with plane-wave DFT. It was found that all Li-PS were thermodynamically unstable as they lay above the tie-line between S and Li₂S [48]. Thus, only one plateau in the discharging curves should be expected. With the same plane-wave DFT method, B. Wang et al. [49] showed the discharging reaction path was altered depending on whether the structures of S (represented as S₈ monomer), Li-PS and Li₂S were modeled as monomers or clusters in a vacuum, both are different from those obtained by treating Li-PS as crystal structures. L. Wang et al. [50] first added the temperature effect due to vibrations and the solvation effect, modeled by polarizable continuum model (PCM), to compute the free energy with local-basis set DFT implemented in Gaussian. Their predicted OCV showed several plateaus. By changing Li, Li₂S, Li-PS from monomer to cluster structures while maintaining the monomer structure of S₈, the predicted OCV curves showed multiple plateaus within the similar voltage range with experimental observation. It is, therefore, reasonable to treat Li-PS as either monomers or clusters [51–53]. However, Li₂S and S should not be treated as dissolved monomer or clusters, as they have very low

solubility in the electrolyte. Furthermore, according to Canepa et al. [54], the calculated solvation energy based on different solvation models might be inconsistent. Including the solvation effect appropriately in the Li-PS system remains another computational challenge. Therefore, a systematic investigation of the influence of the solvation effects at finite temperature on the prediction of OCV is required and important.

In the present work, the primary focus was to understand the origin of the two-plateaued or one-plateaued OCV curves in Li-S batteries. The temperature and solvation effects were added to DFT calculations in order to capture their influence on the OCV profile. The structures used in the model were selected to better mimic the Li-S battery system. Li, S, and Li₂S were treated as crystal structures due to their low solubility in a typical liquid electrolyte and the smallest soluble Li-PS, Li₂S₄ was treated as molecules and clusters. The reason to skip other Li-PS species, such as Li₂S₈, and Li₂S₆, and arguably Li₂S₇ or Li₂S₅ [51,52], in our calculations, is that only one plateau at 2.3–2.4 V was seen in most experiment. That means the OCVs ascribed to the transformation from the crystal S to various Li-PS species will fall into a very narrow energy range, which can be represented by the direct transformation from S to Li₂S₄. The recent eutectic solvent dissolves all Li-PS and Li₂S is interesting but beyond the focus of this paper [55]. The S₃ radical recently observed by Q. Wang et al. [56] was not included in our calculation since it mainly served as a reaction intermedia and would not change the reaction energies that lead to the OCV curve. The mixed electrolyte solvent of dimethoxyethane (DME) and dioxolane (DOL) is often used in Li-S battery. B. Wang et al. [49] suggested that DOL provided slightly larger binding energy to Li-PS than DME. Therefore, DOL was chosen as the electrolyte solvent in our model. It is expected that the solvent-dependent OCV can be extended to other solvents, such as DME, based on different solvation energies. The solvation energies of Li₂S₄ in liquid DOL electrolytes were calculated with different solvation models and the subsequent OCVs from these solvation models were compared with the experimental observations in order to determine which model was more appropriate. This comparison also revealed that the origin of the one-plateaued or two-plateaued discharging curves was due to the solvation of the Li-PS. Thus, the fully solvated, partially solvated, and non-solvated Li₂S₄ were correlated with the design of C/S cathode in the experiment.

Our calculations suggested that a single potential plateau can be expected if the nanopores from carbon matrix create more concentrated and less solvated Li₂S₄ inside the pores than in the bulk electrolyte, or the formation of fully solvated Li₂S₄ is inhibited due to limited amount of solvent in a highly-concentrated electrolyte. For the first time, the theoretical foundation to combine the influence of decreasing pore size and increasing electrolyte concentration on the OCV curve was provided. Based on this, a synergetic effect of the pore size in a carbon matrix and the salt concentration in the electrolyte will result in a transition from the two-plateaued to the one-plateaued. This has been demonstrated in both modeling and systematic experiments. This synergetic effect provides a new strategy to mitigate the Li-PS shuttle problem in Li-S batteries.

2. Method

2.1. OCV and formation energy calculations

The average OCV for a typical lithiation reaction



with reference to Li-metal as 0 V is defined as

$$OCV = \frac{-\Delta G}{\Delta xe} = \frac{-[G(Li_{x2}X) - G(Li_{x1}X) - (x2 - x1)G(Li)]}{(x2 - x1)e}, \quad (2)$$

where ΔG is the change of Gibbs free energy in reaction (1), Δx is the

transferred number of electrons, and e is the charge on one electron. $G(Li_{x_2}X)$, $G(Li_{x_1}X)$ and $G(Li)$ are the Gibbs free energy of phase $Li_{x_1}X$, $Li_{x_2}X$, and Li-metal, respectively. Here, we mainly consider the reaction from S (crystal) $\rightarrow \frac{1}{3}Li_2S_4$ (molecule) $\rightarrow Li_2S$ (crystal). Additional calculations were also performed for other Li-PS molecules, such as Li_2S_8 and Li_2S_6 , to verify the main conclusions. The crystal structures of Li, S, and Li_2S were obtained from the Materials Project [57]. To determine whether the solvated molecular $Li_{2x}S$ would be thermodynamically stable, its formation energy with respect to the crystalline S and Li_2S was calculated as

$$G_{form}(Li_{2x}S) = G(Li_{2x}S) - (1-x)G(S) - xG(Li_2S). \quad (3)$$

A positive $G_{form}(Li_{2x}S)$ means that its formation is not thermodynamically favorable. Thus one step discharging reaction from S crystal to Li_2S crystal, corresponding to the one-plateaued OCV, is expected. On the other hand, if $G_{form}(Li_{2x}S)$ is negative, the formed $Li_{2x}S$ will participate in the two-step discharging reaction and result in a two-plateaued OCV.

For crystalline phases, such as Li, S, and Li_2S , the temperature dependent terms in Gibbs free energy include only the vibration contribution:

$$G(Li_xX_{-crystal}) = E_{DFT}(crystal) + E_{vib}(T) - TS_{vib}(T). \quad (4)$$

For the dissolved molecular, specifically Li_2S_4 in DOL, the Gibbs free energy includes the solvation energy and the temperature dependent contributions of translation, rotation, vibration, of the molecule,

$$G(Li_xX_{-solv}) = E_{DFT}(gas) + [E_{vib}(T) - TS_{vib}(T)] + [E_{rot}(T) - TS_{rot}(T)] + [E_{tra}(T) - TS_{tra}(T)] + E_{solv}. \quad (5)$$

In equation (4) and (5), $E_{DFT}(crystal)$ and $E_{DFT}(gas)$ are the DFT minimized energy of crystals and molecules at 0K. E_{vib} , E_{rot} and E_{tra} are the vibrational, rotational and translational enthalpy, while S_{vib} , S_{rot} and S_{tra} are the vibrational, rotational and translational entropy. E_{solv} is the solvation energy, calculated from different solvation models detailed in Section 2.2.

Because the plane-wave DFT is more efficient for crystals and the local-basis set DFT is the typical choice for molecule and cluster calculations, both were applied to the structures they are suitable for. Comparisons were made to several special cases (crystalline Li, Li_2S , S, and cluster solvation model) for validation purposes. Specifically, spin-polarized, all-electron, local basis set (Double Numerical plus polarization, DNP [58]) DFT implemented in Dmol³ [59] in Materials Studio was used. The exchange-correlation was treated with the generalized gradient approximation (GGA) Perdew-Wang-91 functional [60]. To capture the temperature effect, the contributions from vibration, rotation, and translation were calculated through vibrational analysis by finite differences of analytic gradients, based on the detailed formula from Hirano's work [61]. Only the ion positions were relaxed during energy minimizations, until one of the three convergence criteria, as 3×10^{-4} eV/system energy change, 0.05eV/Å force, and 0.005 Å displacement, was reached. For comparison, the energy of the Dmol³ minimized structures were recalculated with the plane-wave DFT implemented in the Vienna *ab initio* simulation package (VASP). Potentials constructed with the full potential projector augmented wave (PAW) method were used for the elemental constituents [62]. The exchange-correlation was treated with the GGA Perdew-Burke-Ernzerhof (PBE) functional [63]. The cutoff energies and K-points used are listed in Table S1 in the Supporting Information (SI).

2.2. Solvation energy calculations

2.2.1. Solvation models

The solvation energy is the energy associated with dissolving an isolated solute molecule (gas phase) in a solvent to form the solution, which can be calculated as

$$E_{solv} = E[solution] - E[solvent] - E[solute(iso)]. \quad (6)$$

Different solvation models, namely explicit model [64], implicit model [65,66], cluster model [67–69], and combined model [54] are often used in computing solvation energies. In the explicit model, both the solution and the solvent are modeled with full atomistic liquid structures, at the corresponding concentration and density [70,71]. $E[solution]$ and $E[solvent]$ are the average energy obtained from molecular dynamics (MD) or Monte Carlo (MC) simulations. In the implicit model, a single solute molecule embedded in a dielectric continuum media is used to represent the solution. The solute and the solvent interaction can be calculated via the conductor-like screening model (COSMO) [65] or the polarizable continuum model (PCM) [66]. The error for implicit solvation models depends on the dielectric constant, ϵ [72]. The cluster model can be considered as a simplified explicit model, by considering only the first solvation shell [68,69], which can be extracted from liquid structure via MD simulations. Then $E[solution]$ and $E[solvent]$ are the energies of the first solvation shell and the solvent molecule in vacuum, respectively. In the combined model, the first solvation shell is embedded in a dielectric continuum [54], to obtain $E[solution]$ with COSMO or PCM model. $E[solvent]$ is the energy of a solvent molecule

embedded in the dielectric continuum. Comparing these models, the explicit model represents the liquid structure and dynamics properly, but its accuracy is often sacrificed by using classic forcefield. To be more accurate, *ab initio* MD can be used, but with a smaller structure and a shorter time. DFT method is often used for the cluster model, implicit model, and the combined model with DFT method. Considering the cluster model ignores the solvation shell and solvent interaction, the combined model provides a combination of the implicit and cluster model.

In this paper, the solvation energies calculated from these models will be compared. The energetic terms in the explicit model, namely $E[solution]$, $E[solvent]$ and $E[solute(iso)]$, were all calculated through VASP as stated in section 2.1. In the implicit model and combined model, the energetic terms were calculated through Dmol³ with COSMO solvation model [65], in which the solvent was treated as a continuum with a permittivity $\epsilon = 7.2$ for DOL electrolyte [73]. In the cluster model, the energetic terms were calculated in both methods for validation purposes.

2.3. Solution structures

To sample more configurations and save simulation time, classical MD and *ab initio* MD (AIMD) were used to prepare the initial structures for the DFT energy minimizations. While the lowest minimized energies were chosen to calculate the solvation energy, several configurations were used to indicate the fluctuation. The sampling process for Li_2S_4 , as an example, was summarized in Table S2 in SI, and stated in more detail below.

The first solvation shell structure is important for the cluster model and the combined model. The structure of the first solvation shell for a fully solvated Li_2S_4 was obtained from a dilute solution of randomly packed Li_2S_4 and DOL molecules at a ratio of 1:100 simulated by

classical MD. The forcefield types within the Compass [74] and the atomic charges of each atom type were listed in Table S3 in the SI. The optimized cell was subject to a classical MD simulation with an NPT ensemble, using Nosé algorithm [75] and Berendsen algorithm [76] to control the temperature at 298K and pressure at 1 atm for 50 ps with a time step of 1 fs. The MD simulation time was sufficient to give a converged solution density of $1.06 \pm 0.01 \text{ g/cm}^3$ in the last 20 ps. The first solvation shell structure was determined as $\text{Li}_2\text{S}_4\cdot 4\text{DOL}$ by analyzing the radial distribution function (RDF) and the coordination number (CN) around the Li_2S_4 in the MD trajectory. At last, the first solvation shell $\text{Li}_2\text{S}_4\cdot 4\text{DOL}$ was extracted from the three configurations with the lowest potential energy in the MD simulation after equilibrium to be the initial configuration for DFT energy minimization.

To represent the fully solvated solution structure in the explicit model, 1 Li_2S_4 molecule and 20 DOL molecules were packed into the periodic simulation cell with an initial density of 1.06 g/cm^3 . The converged density was $1.19 \pm 0.02 \text{ g/cm}^3$ based on classical NPT MD simulation. This density was 12% higher than the solution with a Li_2S_4 :DOL ratio of 1:100, indicating that this solution deviates from the ideal dilute solution. To better describe the solvent-solute interaction, AIMD implemented in VASP with NVT ensemble at a timestep of 1 fs was performed for 1.5 ps at 300K. The average potential energy during the last 1 ps AIMD simulation were both recorded to obtain the solvation energy and estimate its fluctuation. Three configurations with the lowest potential energy from AIMD simulations were used as the initial configurations for DFT energy minimization.

Explicit and cluster models were chosen to investigate the partially solvated Li_2S_4 . In the explicit model, a solution of 10 Li_2S_4 molecules and 20 DOL molecules were used to simulate a highly-concentrated solution. The converged density averaged from NPT MD simulation was $1.41 \pm 0.014 \text{ g/cm}^3$. After that, a similar process of AIMD and DFT were also followed to obtain the solvent structures for explicit calculations. In the cluster model, a $\text{Li}_2\text{S}_4\cdot 2\text{DOL}$ cluster was created for the first solvation shell of a partially solvated Li_2S_4 by removing 2 DOL molecules from the optimized full solvation shell $\text{Li}_2\text{S}_4\cdot 4\text{DOL}$, then subject to a classical NVT MD simulation at 298K for 50 ps. The configuration with the lowest potential energy was used as the initial configuration for DFT energy minimization.

Non-solvated Li_2S_4 was first simulated as a monomer (isolated molecule). Five different configurations of isolated Li_2S_4 were optimized in DFT calculation. The optimized structure with the lowest energy was chosen to represent the Li_2S_4 monomer. Since non-solvated Li_2S_4 could agglomerate into clusters, Li_2S_4 molecules were arranged under different configurations as $(\text{Li}_2\text{S}_4)_n$ cluster. The initial configurations of larger clusters were built based on the optimized configuration of smaller clusters.

2.4. Experiments

The electrolytes were prepared as follows: lithium bis (trifluoromethane sulphonyl) imide ($\text{LiN}(\text{SO}_2\text{CF}_3)_2$, LiTFSI) salt purchased from TCI was used as received. 1,2-dimethoxyethane (DME) and 1,3-dioxolane (DOL) were obtained from Sigma-Aldrich. 1 M, 3 M and 6 M LiTFSI/(DME + DOL) electrolytes were prepared by dissolving a designed amount of salt into the corresponding solvent. "M" is used to represent the molar concentration, i.e., 1 mol of salt dissolved in a liter of solvent (not the electrolyte solution). The volume ratio of DOL and DME was set to be 1:1 in this work. Three carbon matrixes with different average pore sizes were used. These included CMK3 (average pore size of 5 nm), CMK8 (average pore size of 3 nm) and CMS (average pore size of 1 nm), with pore sizes labeled in the parenthesis, respectively. The carbon/sulfur (S@CMK3, S@CMK8, and S@CMS) composites were prepared by a melting sulfur diffusion method. In detail, a certain amount of carbon matrix and sulfur were uniformly grounded together, sealed in a glass tube under vacuum, and then heated at 155 °C for 15 h. The sulfur loading was 60% for S@CMK3 and S@CMK8, and 50% for

S@CMS.

For the working electrode preparation, carbon/sulfur composite, conductive carbon, polyvinylidene difluoride (PVDF) with a weight ratio of 8:1:1 were mixed in a certain amount of N-methylpyrrolidinone (NMP) solvent to form a homogeneous slurry by stirring for 4 h. The slurry was coated onto a thin Al foil and dried at 65 °C for 14 h in a vacuum.

The coin cells (CR2032) were assembled in an argon-filled glove box, with the prepared working electrode, pure lithium metal foil as the counter electrode, a sheet of polypropylene microporous (PP Celgard) film as the separator. Cyclic voltammetry (CV) measurements were performed on a CHI660D electrochemical workstation with a scan rate of 0.1 mV/s (CH Instrument, Shanghai, China).

3. Results

3.1. Temperature effect in crystalline phases

The calculated energy contributions for all species at both 0 K and 300 K are listed in Table S5 in the SI. At 0 K and 300 K, the vibrational contributions, namely $E_{\text{vib}}(T) - TS_{\text{vib}}(T)$, for crystalline S, Li, and Li_2S , were all less than 0.05 eV. These small vibrational contributions confirmed the typical assumption that the temperature effect for crystals can be neglected in the calculation of the OCV in equation (2) and the relative formation energy (ΔG_{form}) in equation (3). The OCV of the direct reaction of $2\text{Li} + \text{S} = \text{Li}_2\text{S}$ was 2.13 V at 0 K and 2.10 V at 300 K. This confirmed that for OCV calculations in solid, the $T\Delta S$ term in equation (4) was often dropped, as it was relatively much smaller than ΔE at room temperatures for solids [77]. The calculated OCV at 0 K from VASP was 2.04 V. The difference between Dmol3 and VASP method was less than 0.1V, suggesting the results from the two methods can be combined and compared. All of the computed OCV values were in good agreement with most experiments in all solid-state Li-S battery [7,10].

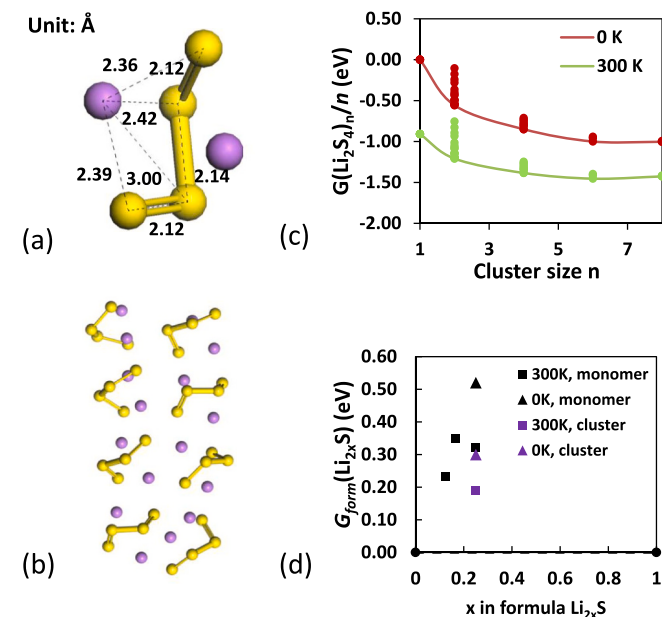


Fig. 1. The structures and formation energies of non-solvated Li-PS. The optimized structure of (a) Li_2S_4 monomer and (b) $(\text{Li}_2\text{S}_4)_8$ cluster. Li and S atom are represented by purple and yellow, respectively. The distance of S-S and S-Li bonds are labeled for Li_2S_4 . (c) The calculated Gibbs free energy of Li_2S_4 , with different configurations, as a function of cluster size n . (d) The predicted relative formation energy of non-solvated Li_2S_4 , Li_2S_6 , and Li_2S_8 with respect to the crystalline S and Li_2S .

3.2. Temperature effect for non-solvated Li_2S_4

However, the temperature effect became significant for molecular Li_2S_4 . The optimized configuration of a non-solvated Li_2S_4 monomer is shown in Fig. 1a. According to Table S5 in SI, the vibrational contribution at 0 K or the zero-point energy (ZPE) was 0.24 eV. At 300K, the free energy contributed from the vibration, rotation, and translation was up to -0.67 eV per Li_2S_4 molecule.

The relative formation energy of Li_2S_4 in the gas phase obtained through equation (3) was 0.52 eV at 0K and 0.33 eV at 300 K. It was observed in the experiment that Li_2S_4 molecules may dynamically aggregate into clusters even at a low concentration of 0.2 M [78]. Therefore, the Gibbs free energy per formula Li_2S_4 , $G_{\text{DFT}}(\text{Li}_2\text{S}_4)_n/n$, was plotted as a function of cluster size n in Fig. 1c. For easy comparison, the Gibbs free energy of Li_2S_4 monomer was shifted to 0. The optimized Gibbs free energy related to different initial configurations were shown as data points. For the monomer, all different initial configurations relaxed into one final configuration. The energy of the dimers showed large dependence on the initial configurations. The larger clusters built upon the lowest energy dimers showed less fluctuation in the minimized energy. The lowest energies clearly showed that $G_{\text{DFT}}(\text{Li}_2\text{S}_4)_n/n$ decreased with increasing cluster size till it converged within 0.05 eV when n is larger than 6. Therefore, the optimized structure of $(\text{Li}_2\text{S}_4)_8$ cluster, as shown in Fig. 1b, was chosen to represent the Li_2S_4 cluster in a vacuum. The difference between Gibbs free energy at 0K and 300K also dropped from 1eV to 0.4eV with increasing cluster size. These results suggested that the temperature effect on free energy cannot be ignored for the Li_2S_4 molecule or clusters, thus the following calculation mainly focused on the Gibbs free energy at 300 K.

Fig. 1d plots the relative formation energies of non-solvated Li_2S_4 , Li_2S_6 , and Li_2S_8 with respect to a tie line between the crystalline S and Li_2S . As discussed in Section 3.1, the temperature effect (from 0 K to 300 K) on the Gibbs free energy of crystalline S and Li_2S was negligible and thus the position of the tie line can be treated as a constant. The relative formation energy of the non-solvated Li_2S_4 cluster was therefore 0.30

eV at 0 K and 0.19 eV at 300 K. Regardless of monomer or cluster, the relative formation energy of Li_2S_4 remained positive without the solvent. Li_2S_6 and Li_2S_8 monomers also showed positive relative formation energies at 300 K with respect to S and Li_2S , indicating all Li-PS including Li_2S_4 , Li_2S_6 and Li_2S_8 should not form. Consequently, a one-plateaued discharging curve was expected.

3.3. Fully solvated Li_2S_4

For the cluster model and combined model, the first solvation shell of $\text{Li}_2\text{S}_4 \cdot 4\text{DOL}$ (Fig. 2a) was extracted based on classical MD simulations of 1 Li_2S_4 in 100 DOL by analyzing the RDF and the CN around the Li_2S_4 . Fig. 2b shows the cumulative CN as a function of the cutoff distance for the Li-O distance. The two CN steps meant that each Li^+ in the Li_2S_4 coordinated with 2 DOL molecules via Li-O ionic bond at ~ 2 Å, and the second nearest Li-O neighbors were ~ 4 Å away. To further differentiate the Li-S bonds, the two S atoms at the end of S_4^{2-} anion were defined as S (end) and the two S atoms in the middle were defined as S (mid). Each Li^+ in the Li_2S_4 also formed ionic bonds with the two S (end) at ~ 2.4 Å. Thus, the first solvation shell was $\text{Li}_2\text{S}_4 \cdot 4\text{DOL}$, in which each Li at the end of Li_2S_4 was coordinated to 2 O atoms from two different DOL molecules at a distance around 2 Å.

The liquid solution model (shown in Fig. 2c) used for AIMD calculations had one Li_2S_4 and 20 DOL molecules. The first solvation shell around the Li_2S_4 is highlighted in Fig. 2c and its cumulative CN is shown in Fig. 2d, which had exactly the same first nearest neighbor bonding and CN as that from the larger liquid simulation cell shown in Fig. 2b, except the Li-O CN kept increasing after 4 Å. This suggested that the first solvation shell was consistent with the large cells but the second solvation shell was not fully formed in the AIMD simulation cell.

Table 1 compares the four different solvation models utilized to calculate the solvation energy for a fully solvated Li_2S_4 molecule. At 300 K, the Gibbs free energy of the fully solvated Li_2S_4 monomer, regardless the solvation model, was lower than that of the non-solvated $(\text{Li}_2\text{S}_4)_8$ cluster, suggesting that formation of clusters of Li_2S_4 in dilute solution

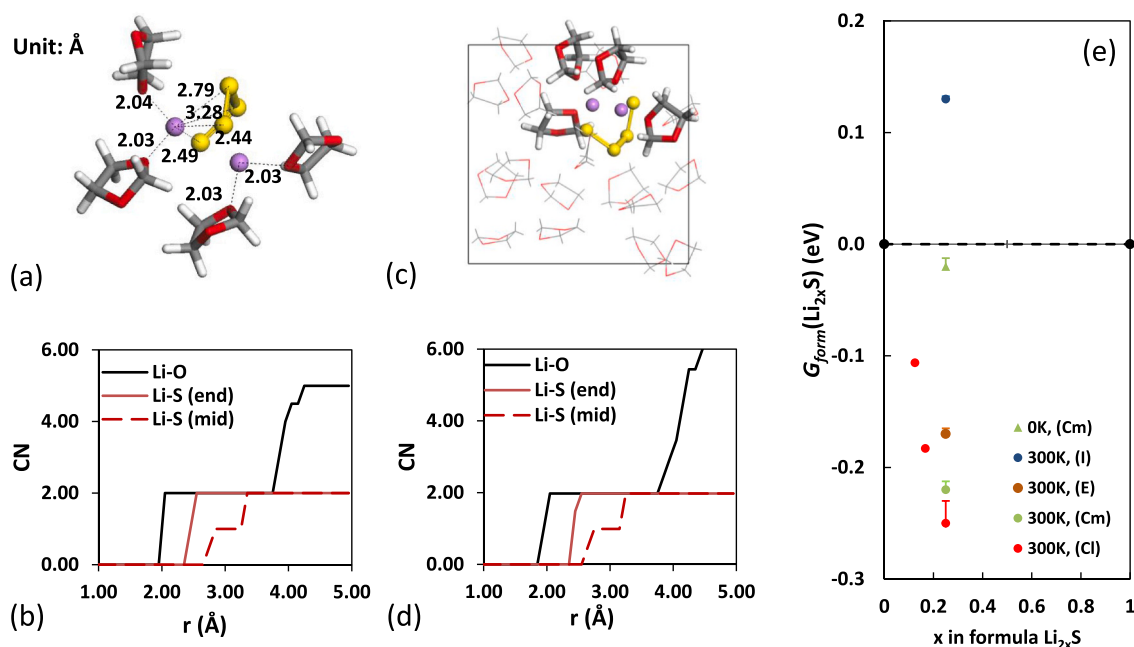


Fig. 2. The solvation structure and energy for the fully solvated Li-PS monomer. The optimized configuration of $\text{Li}_2\text{S}_4 \cdot 4\text{DOL}$ solvation shell and their cumulative CN in (a)(b) the cluster model and (c)(d) the explicit model. The Li, S, C, O, and H are represented as purple, yellow, grey, red and white, respectively. The distance of Li-S and Li-O are labeled. The relative formation energy of the fully solvated Li_2S_4 monomer at 0 K and 300 K, and fully solvated Li_2S_6 and Li_2S_8 at 300 K compared with crystalline S and Li_2S (e). The labels indicate the temperature, and the solvation model, namely (I) for implicit, (Cl) for cluster, (Cm) for combined, and (E) for explicit models, respectively. The error bar indicates the results due to a range of sampled configurations.

Table 1

E_{solv} for the fully and partially solvated Li_2S_4 in DOL solvent calculated by different solvation models (Unit: eV). The fluctuations are due to different configurations in the sampling scheme.

		Implicit Model	Explicit Model	Cluster Model	Combined Model
Fully solvated	Dmol3	-0.80		-2.27	-2.16
	VASP	[+0.01]		[+0.08]	[+0.03]
Partially solvated	Dmol3		-1.91	-1.43	
	VASP		[+0.02]	[+0.08]	
			-1.44	-1.30	
			[+0.03]		

was not energetically favorable, although it was reported that they dynamically exist [78] in the electrolyte or energetically favorable on the Li anode surface [79]. Thus, only a solvated monomer of Li_2S_4 was considered further to mimic the solvated Li-PS.

The solvation energy calculated by the implicit model was only -0.80 eV, much smaller than that calculated by the other three models, falling into the range of -2.09 ± 0.18 eV. In the cluster model, a difference of 0.22 eV in the solvation energy calculated by VASP and Dmol3 was also observed. This difference was within the same level of the deviation caused by different solvation models, expect the implicit model.

Fig. 2e shows the relative formation energy of the fully solvated Li-PS monomers, predicted by different solvation models. The cluster model, explicit model, and the combined model all predicted negative relative formation energies for the fully solvated Li_2S_4 at 300K, within a range from -0.17 eV to -0.25 eV. This suggested that the fully solvated Li_2S_4 was a thermodynamically stable product in the discharging reaction. The fully solvated Li_2S_8 and Li_2S_6 also showed negative formation energies (using the cluster model). Since the formation energy of S crystal, fully solvated Li_2S_8 , Li_2S_6 and Li_2S_4 almost resided on the same line, the slope of this line resulted in the same discharge potential plateau of ~ 2.43 V. The phase change from fully solvated Li_2S_4 to crystalline Li_2S led to another OCV plateau of, thus the two-plateaued OCV was expected. This was in agreement with most experiment observations in typical Li-S batteries with liquid electrolytes [3,6]. The solvation energy deviation of ± 0.18 eV due to different solvation models and calculation methods only caused less than ± 0.1 V shift of the discharging plateaus, deemed to be acceptable. On the other hand, the positive relative formation energy predicted by the implicit model at 300 K (0.13 eV) led to an inaccurate conclusion, that the fully solvated Li_2S_4 was not thermodynamically stable, which was against the experimental observations. Thus, the implicit solvation model was not appropriate for the solvation energy calculation of Li_2S_4 in DOL solvent. The single plateau for all dissolved Li-PS phases verified our previous decision that Li_2S_4 can be used to represent all Li-PS for OCV calculations. So the rest of the calculations only focused on Li_2S_4 at different solvation states.

Fig. 2e also shows the temperature effect on the relative formation energy of the fully solvated Li_2S_4 monomer. The relative formation energy was only -0.02 eV at 0 K (considering the solvation energy with the combined model and the ZPE). The slightly negative value indicated the two discharging plateaus would be very close, almost overlapping, on the OCV. Thus, the temperature had a significant effect on the OCV of reactions involving dissolved molecules. These results also suggested that the voltage difference on OCV decreased with temperature, thus lowering the operating temperature might be helpful to mitigate the Li-PS desolvation problem.

3.4. Partially solvated Li_2S_4 and the transition from the two-plateaued OCV to the one-plateaued OCV

The partially solvated Li_2S_4 may exist in high concentration solutes.

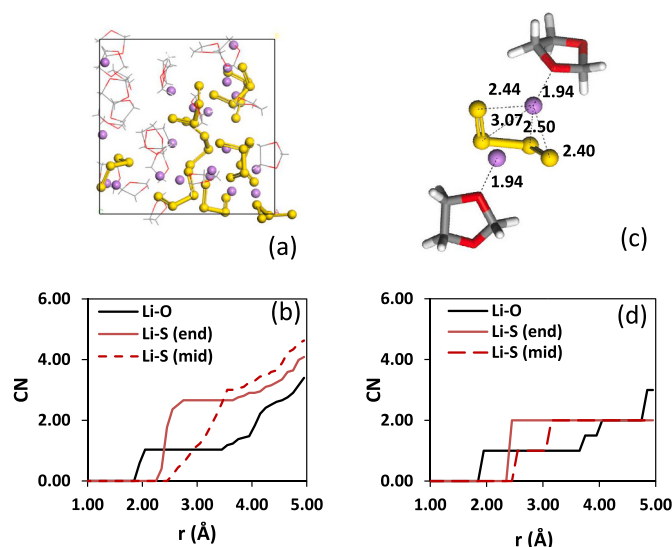


Fig. 3. Structures of the partially solvated Li_2S_4 . (a) The liquid structure of $10\text{Li}_2\text{S}_4\cdot 20\text{DOL}$ in the explicit model and (c) the $\text{Li}_2\text{S}_4\cdot 2\text{DOL}$ solvation shell in the cluster model, along with their cumulative CN as a function of cutoff radius in (b) and (d), respectively. The color code is the same as Fig. 2.

A liquid simulation cell of $10 \text{Li}_2\text{S}_4$ and 20DOL was used for the explicit solvation model. The solution structure after 2 ps AIMD simulations and its corresponding CN plots are shown in Fig. 3a and b. Comparing Fig. 3b with the fully solvated Li_2S_4 in Fig. 2c, the first nearest neighbor Li-O and Li-S (end) bonds almost maintained the same distance. However, the coordination number changed. In the partially solvated Li_2S_4 , each Li^+ was coordinated with 1 O in DOL but coordinated with more S (end) with $\text{CN} = 2.7$. The continuous climbing of all bonds beyond the distance of 3.5Å , indicating the second solvation shell was not fully formed. The change of CN in the highly-concentrated solution strongly suggested that the interaction between DOL and Li^+ was weakened due to the limited amount of DOL, while the interaction between S_4^{2-} and Li^+ was enhanced by the formation of a Li-PS network as shown from the snapshot in Fig. 3b. A cluster of $\text{Li}_2\text{S}_4\cdot 2\text{DOL}$ was used to represent the partial solvation shell in the cluster model. The optimized structure and its corresponding CN plot are shown in Fig. 3c and d, which shows the CN of the Li-O, Li-S (end) and Li-S (mid) bonds was 1, 2 and 1, respectively, similar to that in Fig. 3b.

The calculated partial solvation energies from VASP were -1.44 eV from the explicit model and -1.30 eV from the cluster model. For comparison, the calculated solvation energy from Dmol3 was -1.43 eV with the cluster model. These consistent solvation energies for the partially solvated Li_2S_4 were smaller (in the absolute value) than the -2.09 eV solvation energy of a fully solvated Li_2S_4 . The corresponding formation energy of the partially solvated Li_2S_4 was -0.01 to -0.04 eV, recommending two-plateaued OCVs. But since these values were close to zero, these voltages of the two plateaus would fall into a very narrow range.

3.5. Synergy effect of pore size and salt concentration on the OCVs

The relative formation energies at 300K for the fully solvated Li_2S_4 , partially solvated Li_2S_4 , and non-solvated Li_2S_4 are summarized in Fig. 4a. The solvation energy for the fully solvated Li_2S_4 was represented as the average value of -2.09 eV from the cluster model, combined model and explicit model shown in Table 1, resulting a relative formation energy of -0.22 eV shown as the green dot in Fig. 4a. A solvation energy of -0.03 eV was also obtained by averaging the values of the cluster and explicit model for the partially solvated Li_2S_4 , leading to a relative formation energy of -0.05 eV shown as the blue dot in Fig. 4a.

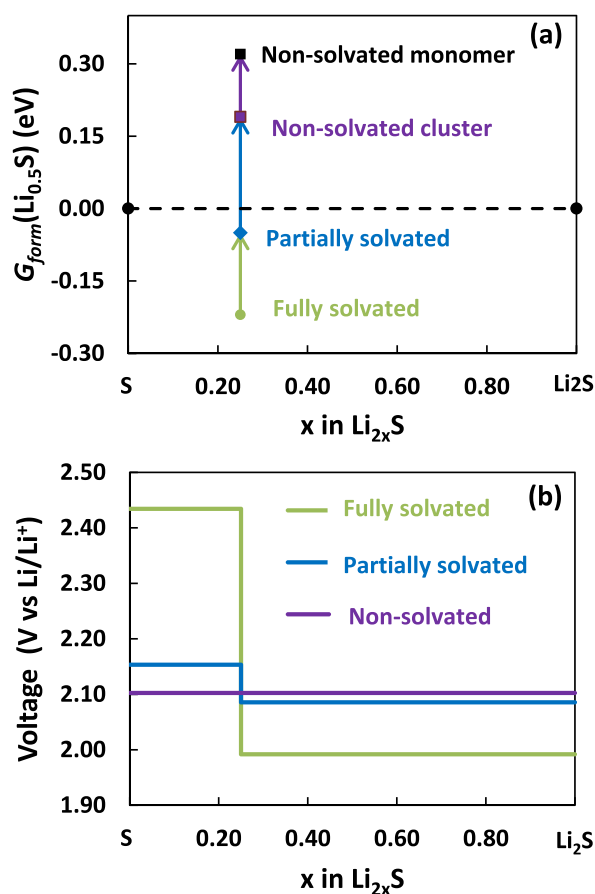


Fig. 4. The calculated (a) relative formation energies and (b) the corresponding OCVs for Li_2S_4 in different solvation status at 300K. The energy of crystalline S and Li_2S are already shifted to 0 for easy comparison in (a).

The non-solvated Li_2S_4 was represented as an isolated Li_2S_4 monomer shown as a black dot and isolated $(Li_2S_4)_8$ cluster shown as a purple dot, separately. They both led to positive relative formation energy. The resulted OCVs based on the relative formation energies at 300K are shown in Fig. 4b.

The one-plateaued OCV was predicted for non-solvated Li_2S_4 . The discharging plateau, attributed to the single step discharging reaction of $2Li + S = Li_2S$, was 2.11 V. This was in good agreement with most experiments in all solid-state Li-S batteries [7–9]. This prediction was also valid with carbonate electrolyte when S was sealed inside of carbon pores by *in-situ* formed SEI [36,80]. Therefore, carbonate electrolytes were suitable for nano-porous carbon/sulfur cathodes. The two-plateaued OCV was predicted for fully solvated Li_2S_4 . The voltages of the two plateaus predicted to be 2.43 V and 1.99, were in agreement with the experimental observation in general Li-S battery with ether-based liquid electrolyte without any special design [3–6]. If Li_2S_4 is fully solvated in the electrolyte, especially when the pores are at the micron level, it is subject to severe Li-PS shuttle problems. In such a case, the solubility of the Li-PS in the electrolyte in microporous carbon/sulfur electrode becomes one of the key parameters affecting the electrochemical performance and energy density of the Li-S batteries, as shown in our previous analytical model [81].

For partially solvated Li_2S_4 , the increase of partial solvation energy made the two plateaus on the OCV much closer, as the first plateau dropped to 2.15 V while the second plateau increased to 2.09 V. Further increase in the Li_2S_4 concentration in DOL would eventually create a single plateaued OCV. This was consistent with experimental observations in concentrated electrolyte [24–26]. Especially, Zhang [24] has also shown that while the second discharging plateau almost maintained

the same position, the first discharging plateau gradually dropped when the concentration of the electrolyte increased. This would be an efficient method to avoid Li-PS dissolution. When the Li-salt concentration in the electrolyte increases, the amount of free solvent molecules drops dramatically as more solvent molecules are needed in forming the Li-ion solvation shell. Thus, there will be less free solvent molecules available to form full solvation shells around the newly generated Li-PS. The partially solvated Li-PS can continue to be lithiated while reducing the amount of Li-PS that can shuttle through the electrolyte. In the experiment, the cycling performance is generally improved with the use of highly concentrated electrolyte [25].

The structure of C/S cathode with S filled nano-pores will impact the local solvation structure of Li-PS. If the pore size is large enough for the first solvation shell $Li_2S_4 \cdot 4DOL$ to pass, the pores will not impose any constraints on the electrolyte concentration or diffusion, leading to severe Li-PS shuttle problems. The size of $Li_2S_4 \cdot 4DOL$ is ~ 1 nm as shown in Fig. 2a. Thus, extremely small pores on the order of ~ 1 nm will allow Li^+ diffusion while limiting the diffusion of DOL molecules and blocking the diffusion of $Li_2S_4 \cdot 4DOL$ solvation shell. If any Li_2S_4 can be formed inside these pores, it will likely exist as a non-solvated monomer or cluster, leading to a one-plateaued OCV. Several experiments indeed have created nanopore size on the order ~ 1 nm and reported one-plateaued discharging curves in the liquid electrolyte [14,82]. We hypothesize that partial solvation can be achieved inside the pores within the size range of 1–5 nm, where both Li-ion and solvent molecules can diffuse in, but the diffusion of the newly formed $Li_2S_4 \cdot 4DOL$ solvation shell out of the pore will be limited, due to the comparable size of solvation shell and pore size. This was similar to the reverse osmosis phenomena in graphene membrane with similar pore size for water desalination [83]. This can create a local higher Li-PS concentration and result in a partially solvated state inside the pore. The formation of Li_2S_4 will become less energetically favorable with increasing Li_2S_4 concentration. This explains why some so called “quasi one-plateaued” discharging curves were still displayed when the pore size was much larger than the size of the solvent [17,35–37]. Also, due to the limited amount of solvent, the diffusion of Li_2S_4 into electrolyte will also be hindered. As a result, fewer Li-PS will be involved in the PS shuttle, mitigating Li-PS shuttle problem.

As discussed above, solely decreasing pore size in carbon matrix [23, 24,34] with standard concentration of electrolyte, or solely using highly concentrated electrolyte (generally above 5 M) with large pore size in carbon matrix [17,35–37], as done in many previous researches faced extreme challenges due to costly synthesis process and slow Li-ion transport property. The significance of our model is that, for the first time, the influences of decreasing pore size and increasing electrolyte concentration on the OCV could be successfully combined, since they can both help to create a partially solvated Li-PS in a liquid electrolyte. Based on this, we proposed that the most efficient method to limit the PS dissolution problem is to take advantage of the synergetic effect between pore size and electrolyte concentration, which provided a new strategy to convert the two plateaued discharging curves to one plateaued discharging curves and mitigate the PS dissolution.

To confirm the synergetic effect between pore size and electrolyte concentration, Li-S batteries made of LiTFSI/(DME + DOL) electrolyte systems in the concentration range of 1 M–6 M along with the S@CMS cathode with nanopores size ranging from 1 nm to 5 nm have been assembled and tested. Fig. 5a, shows the cyclic voltammograms (CV) at the 5th cycle in 1 M LiTFSI/(DME + DOL) electrolyte with S@CMK3 (5 nm) S@CMK8 (3 nm) and S@CMS (1 nm) cathode, respectively. The corresponding galvanostatic discharging curves are shown with the same color in Fig. s1a, and the full CV curves from 1st to 5th cycle are displayed in Figs. s2a–c in the supporting materials. For S@CMK3 and S@CMK8, the two reduction peaks were distinctly observed in Fig. 5a. This was consistent with the typical two-plateaued discharging curves shown in green and red in Fig. s1a. Furthermore, the two reduction peaks for S@CMK8 with the average pore size of 3 nm were closer than that for S@CMK3 with 5 nm pores. For the S@CMS with 1 nm pore, the

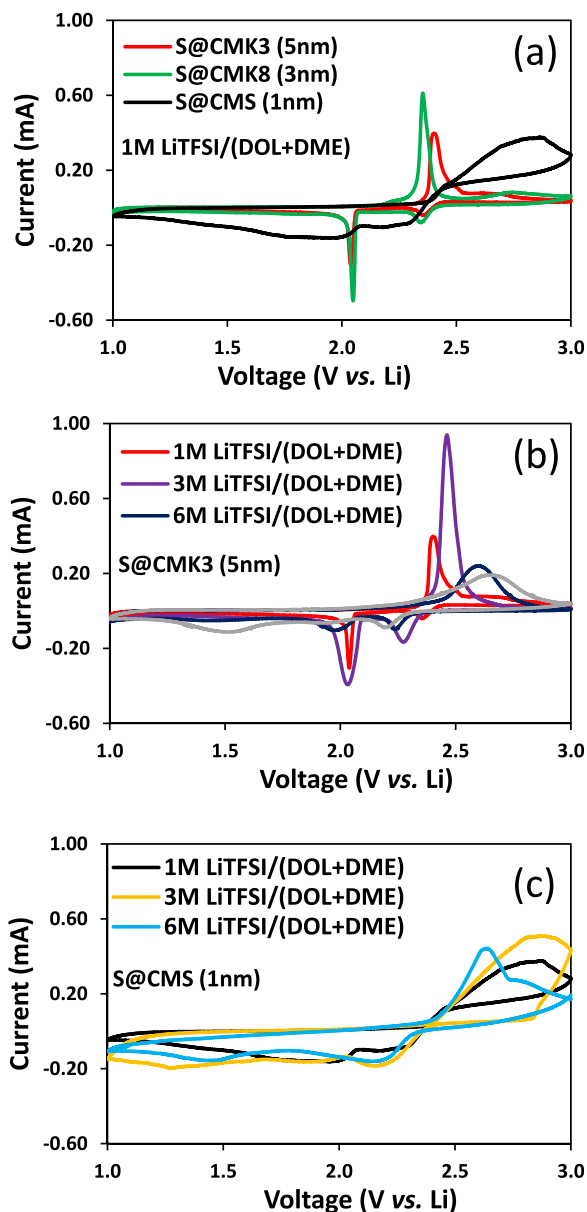


Fig. 5. Cyclic voltammograms and galvanostatic discharging curve of Li-S batteries. (a) CV in 1 M LiTFSI/(DME + DOL) electrolyte paired with cathodes with different carbon matrix pore sizes (labeled in parenthesis), S@CMK3, S@CMK8, and S@CMS, respectively. (b) galvanostatic discharging curves of S@CMK3 cathode in LiTFSI/(DME + DOL) electrolyte at concentrations of 1 M, 3 M, 6 M and 9 M. (c) galvanostatic discharging curves of S@CMS cathode in LiTFSI/(DME + DOL) electrolyte at concentrations of 1 M, 3 M and 6 M. The cyclic voltammograms were tested with a sweep rate of 0.1 mV/s at the 5th cycle. The galvanostatic discharging curves were tested at a 0.1C rate in the 10th cycle.

two peaks became broader. The corresponding black discharging curve in Fig. s1a also showed two much closer discharging plateaus. Thus, the experimental results confirmed the prediction that the two reduction plateaus will move closer with decreasing pore sizes of the carbon matrix.

The galvanostatic discharging curves of S@CMK3 and S@CMS cathode at the 10th cycle in LiTFSI/(DME + DOL) electrolyte with different concentrations are shown in Fig. 5b and c. The corresponding CV curves in the 5th cycle are shown with the same color in Figure s1b and s1c, and the full CV curves from the 1st to 5th cycle are displayed in Figure s2c ~ h in the supporting materials. For S@CMK3 with 5 nm

pore, when the electrolyte concentration increased from the 1 M–3 M, the two plateaus in Fig. 5b and the two peaks in Figure s1b became closer. This confirmed our prediction that an increase of salt concentration in the electrolyte can also make the two reduction plateaus closer. In even highly concentrated 6 M and 9 M electrolytes, the discharging curves shown as dark blue and grey in Fig. 5b gradually showed a gradual transition to the one-plateaued type. This was also consistent with the broad CV peaks in Figure s1b. For S@CMS with 1 nm pores, complete one plateaued discharging curves were displayed for 3 M and 6 M electrolytes, shown as yellow and light blue in Fig. 5c. One broad CV peak in the entire range of reduction can be seen in Figure s1c. The use of CMS with 1 nm pores reduced the critical electrolyte concentration to 3 M, above which a one-plateaued OCV was observed, confirming the synergetic effect of pore size and electrolyte concentration. The use of 3 M electrolyte can facilitate faster Li transport in the electrolyte, compared with that in a 6 M or 9 M electrolyte. The use of 1 nm pore, can also form a higher local concentration of Li or Li-PS and create a partially solvated Li-PS inside the pore. The combining effect will mitigate the Li-PS shuttling problem more efficiently, compared with the use of a 3 nm or 5 nm pore size. The combination of the 3 M electrolyte and 1 nm pore provided a new strategy to convert the two plateaued discharging curves to one plateaued discharging curves and mitigate the Li-PS dissolution.

It was worth noting that the second plateau of all galvanostatic discharging curves in Fig. 5b and c and s1a became quite sloped when the state of discharge was higher than 70%. This was due to the increasing overpotential due to the continuous deposition of the insulating $\text{Li}_2\text{S}_2/\text{Li}_2\text{S}$ layer [84].

It was worth emphasizing here that our primary focus in this research was to understand the origin of the two-plateaued and one-plateaued discharging curves in the typical ether-based electrolyte and achieve one-plateaued discharging curves through the synergetic effect between decreasing pore size and increasing electrolyte concentration. Even though much previous research showed that the cycling stabilities of Li-S batteries displaying one-plateaued OCV curves were much better than that with two-plateaued OCV curves [20,23–25,28–32], future characterizations are still needed to confirm the influence of the synergetic effect on the cycling stability. Furthermore, some insights are also expected from our calculation for the design of new electrolytes. Smaller solvation energy due to weaker interaction between the solvent and Li-PS should be helpful to mitigate the Li-PS dissolution. In such a case, the fully solvated Li-PS will not be energetically favorable even at low concentrations. This is consistent with the concept of sparingly solvated electrolytes [85]. Furthermore, liquid electrolyte structure with nano-heterogeneity [86], promoting the Li diffusion in the concentrated electrolytes, can be further explored to enhance the rate performance.

4. Conclusions

In summary, we have devised a method based on density functional theory (DFT) calculations to predict the temperature and solvent dependent OCV when both crystals (S, Li_2S , Li) and dissolved molecules (Li-PS, such as Li_2S_4) are involved in the discharging reaction. The energies of S, Li_2S , Li crystal, and Li_2S_4 molecule were successfully calculated and combined with consistent results from plane-wave DFT and basis set DFT. The temperature and solvation effect on the predicted free energy and the open circuit voltage (OCV) curves for Li-S batteries were systematically investigated. It was also shown that while the effect of temperature was negligible for predicting OCV curves associated only with solid-phase transformation, it played a deterministic role in the free energy of dissolved molecules, such as Li-PS. The consistency in the solvation structure and solvation energy in different models confirmed that the solvation effect was estimated appropriately. With the appropriate treatment of temperature and solvation effect, we successfully predicted two-plateaued OCV with fully solvated Li_2S_4 and one-plateaued OCV with non-solvated Li_2S_4 , in agreement with

experimental observation in typical Li-S battery with liquid or solid electrolytes.

Driven by the modeling, it was also predicted that the relative formation energy of Li_2S_4 increased in the order of fully solvated Li_2S_4 , partially solvated Li_2S_4 and non-solvated Li_2S_4 . Thus, the transition from two-plateaued to one-plateaued discharging curves was attributed to the change of the solvation state of the Li-PS. At last, the fully solvated, partially solvated, and non-solvated Li_2S_4 were correlated with the design of C/S cathode by the varying pore size of the carbon matrix in the experiment. A new mechanism that nanopores from carbon matrix can create concentrated and partially solvated Li_2S_4 inside was proposed. For the first time, the theoretical foundation was provided to combine the influence of decreasing pore size and increasing electrolyte concentration on the OCV curve. Based on this, a synergetic effect of pore size in carbon matrix and salt concentration in the electrolyte in the conversion from two-plateaued and one-plateaued discharging curves was predicted and also confirmed through experiments.

Author contributions

The manuscript was written through the contributions of all authors.

Funding sources

U.S. Department of Energy, Office of Science, Basic Energy Sciences under Award number DESC0001160.

Declaration of competing interest

The authors declare no conflict of interest.

CRedit authorship contribution statement

Yuxiao Lin: Conceptualization, Methodology, Investigation, Writing - original draft, Writing - review & editing. **Jing Zheng:** Methodology, Validation, Writing - review & editing. **Chunsheng Wang:** Conceptualization, Methodology, Supervision, Writing - review & editing. **Yue Qi:** Conceptualization, Methodology, Supervision, Writing - original draft, Writing - review & editing.

Acknowledgment

We acknowledge the support for degradation mechanism modeling as part of Nanostructures for Electrical Energy Storage (NEES), an Energy Frontier Research Center funded by the U.S. Department of Energy, Office of Science, Basic Energy Sciences under Award number DESC0001160.

Appendix A. Supplementary data

Supplementary data to this article can be found online at <https://doi.org/10.1016/j.nanoen.2020.104915>.

References

- [1] M.-K. Song, E.J. Cairns, Y. Zhang, *Nanoscale* 5 (2013) 2186.
- [2] J. Lochala, D. Liu, B. Wu, C. Robinson, J. Xiao, *ACS Appl. Mater. Interfaces* 9 (2017) 24407–24421.
- [3] D.-W. Wang, Q. Zeng, G. Zhou, L. Yin, F. Li, H.-M. Cheng, I.R. Gentle, G.Q.M. Lu, *J. Mater. Chem. A* 1 (2013) 9382–9394.
- [4] S.S. Zhang, *J. Power Sources* 231 (2013) 153–162.
- [5] R. Dominko, A. Vizintin, G. Aquilanti, L. Stievano, M.J. Helen, R. Munnangi, M. Fichtner, *Isl. Arc* 165 (2018) 5014–5019.
- [6] S. Talian, S. Jeschke, A. Vizintin, K. Pirnat, G. Aquilanti, P. Johansson, R. Dominko, *Chem. Mater.* 29 (2017) 10037–10044.
- [7] C. Zhang, Y. Lin, J. Liu, *J. Mater. Chem.* 3 (2015) 10760–10766.
- [8] Y. Zhang, T. Liu, Q. Zhang, X. Zhang, S. Wang, X. Wang, L. Li, L.Z. Fan, C.W. Nan, Y. Shen, *J. Mater. Chem. A* 6 (2018) 23345–23356.
- [9] X. Fan, X. Ji, F. Han, J. Yue, J. Chen, L. Chen, T. Deng, J. Jiang, C. Wang, *Sci. Adv.* 4 (2018) eaau9245.
- [10] Z. Lin, Z. Liu, W. Fu, N.J. Dudney, C. Liang, *Angew. Chem. Int. Ed.* 52 (2013) 7460–7463.
- [11] E. Markevich, G. Salitra, Y. Talyosef, F. Chesneau, D. Aurbach, *J. Electrochem. Soc.* 164 (2017) A6244–A6253.
- [12] L. Qie, W.M. Chen, Z.H. Wang, Q.G. Shao, X. Li, L.X. Yuan, X.L. Hu, W.X. Zhang, Y. H. Huang, *Adv. Mater.* 24 (2012) 2047–2050.
- [13] B. Zhang, X. Qin, G.R. Li, X.P. Gao, *Energy Environ. Sci.* 3 (2010) 1531.
- [14] A. Rosenman, E. Markevich, G. Salitra, Y. Talyosef, F. Chesneau, D. Aurbach, *J. Electrochem. Soc.* 163 (2016) A1829–A1835.
- [15] M.R. Busche, P. Adelhelm, H. Sommer, H. Schneider, K. Leitner, J. Janek, *J. Power Sources* 259 (2014) 289–299.
- [16] D. Lei, K. Shi, H. Ye, Z. Wan, Y. Wang, L. Shen, B. Li, *Adv. Funct. Mater.* 28 (2018) 1707570.
- [17] X. Ji, K.T. Lee, L.F. Nazar, *Nat. Mater.* 8 (2009) 500–506.
- [18] O. Ogoke, G. Wu, X. Wang, A. Casimir, L. Ma, T. Wu, J. Lu, *J. Mater. Chem.* 5 (2017) 448–469.
- [19] D.-W. Wang, G. Zhou, F. Li, K.-H. Wu, G. Q. (Max) Lu, H.-M. Cheng, I.R. Gentle, *Phys. Chem. Chem. Phys.* 14 (2012) 8703.
- [20] Y. Zhou, C. Zhou, Q. Li, C. Yan, B. Han, K. Xia, Q. Gao, J. Wu, *Adv. Mater.* 27 (2015) 3774–3781.
- [21] Y. Xu, Y. Wen, Y. Zhu, K. Gaskell, K.A. Cychosz, B. Eichhorn, K. Xu, C. Wang, *Adv. Funct. Mater.* 25 (2015) 4312–4320.
- [22] X. Li, M. Bani, A. Lushington, X. Yang, Q. Sun, Y. Zhao, C. Liu, Q. Li, B. Wang, W. Xiao, et al., *Nat. Commun.* 9 (2018) 4509.
- [23] S. Xin, L. Gu, N.H. Zhao, Y.X. Yin, L.J. Zhou, Y.G. Guo, L.J. Wan, *J. Am. Chem. Soc.* 134 (2012) 18510–18513.
- [24] M. Helen, M.A. Reddy, T. Diemant, U. Golla-Schindler, R.J. Behm, U. Kaiser, M. Fichtner, *Sci. Rep.* 5 (2015) 12146.
- [25] T. Fujimori, A. Morelos-Gómez, Z. Zhu, H. Muramatsu, R. Futamura, K. Urita, M. Terrones, T. Hayashi, M. Endo, S. Young Hong, et al., *Nat. Commun.* 4 (2013) 1–8.
- [26] J. Chen, K.S. Han, W.A. Henderson, K.C. Lau, M. Vijayakumar, T. Dzwiniel, H. Pan, L.A. Curtiss, J. Xiao, K.T. Mueller, et al., *Adv. Energy Mater.* 6 (2016) 1–6.
- [27] J.-W. Park, K. Yamauchi, E. Takashima, N. Tachikawa, K. Ueno, K. Dokko, M. Watanabe, *J. Phys. Chem. C* 117 (2013) 4431–4440.
- [28] Y.Z. Zhang, S. Liu, G.C. Li, G.R. Li, X.P. Gao, *J. Mater. Chem.* 2 (2014) 4652–4659.
- [29] L. Suo, Y.-S. Hu, H. Li, M. Armand, L. Chen, *Nat. Commun.* 4 (2013) 1481.
- [30] D. Lv, P. Yan, Y. Shao, Q. Li, S. Ferrara, H. Pan, G.L. Graff, B. Polzin, C. Wang, J. Zhang, et al., *Chem. Commun.* 51 (2015) 13454–13457.
- [31] J. Zheng, X. Fan, G. Ji, H. Wang, S. Hou, K.C. DeMella, S.R. Raghavan, J. Wang, K. Xu, C. Wang, *Nano Energy* 50 (2018) 431–440.
- [32] J. Zhou, Y. Guo, C. Liang, L. Cao, H. Pan, *Chem. Commun.* 54 (2018) 5478–5481.
- [33] G. Zhou, S. Zhao, T. Wang, S. Yang, B. Johannessen, H. Chen, C. Liu, Y. Ye, Y. Wu, Y. Peng, et al., *Nano Lett.* 20 (2019) 1252–1261.
- [34] Z. Li, Y. Jiang, L. Yuan, Z. Yi, C. Wu, Y. Liu, P. Strasser, Y. Huang, *ACS Nano* 8 (2014) 9295–9303.
- [35] J.T. Lee, K. Eom, F. Wu, H. Kim, D.C. Lee, B. Zdyrko, G. Yushin, *ACS Energy Lett.* 1 (2016) 373–379.
- [36] E. Markevich, G. Salitra, A. Rosenman, Y. Talyosef, F. Chesneau, D. Aurbach, *Electrochem. Commun.* 60 (2015) 42–46.
- [37] B. Zhang, C. Lai, Z. Zhou, X.P. Gao, *Electrochim. Acta* 54 (2009) 3708–3713.
- [38] C. Fang, X. Wang, Y.S. Meng, *Trends Cognit. Sci.* 1 (2019) 152–158.
- [39] Y. Zhang, Y. Zhong, Q. Shi, S. Liang, H. Wang, *J. Phys. Chem. C* 122 (2018) 21462–21467.
- [40] R. Miao, J. Yang, Z. Xu, J. Wang, Y. Nuli, L. Sun, *Sci. Rep.* 6 (2016) 2–10.
- [41] L. Suo, O. Borodin, T. Gao, M. Olguin, J. Ho, X. Fan, C. Luo, C. Wang, K. Xu, *Science* 350 (2015) 938.
- [42] X. Dong, Z. Guo, Z. Guo, Y. Wang, Y. Xia, *Joule* 2 (2018) 902–913.
- [43] Y.S. Meng, M.E. Arroyo-de Dompablo, *Energy Environ. Sci.* 2 (2009) 589.
- [44] S.P. Ong, V.L. Chevrier, G. Hautier, A. Jain, C. Moore, S. Kim, X. Ma, G. Ceder, *Energy Environ. Sci.* 4 (2011) 3680.
- [45] Y. Yamaguchi, T. Takeuchi, H. Sakaebe, H. Kageyama, H. Senoh, T. Sakai, K. Tatsumi, *J. Electrochem. Soc.* 157 (2010) A630.
- [46] I.A. Courtney, J.S. Tse, O. Mao, J. Hafner, J.R. Dahn, *Phys. Rev. B Condens. Matter* 58 (1998) 15583–15588.
- [47] H. Okamoto, *J. Phase Equil.* 16 (1995) 94–97.
- [48] G. Yang, S. Shi, J. Yang, Y. Ma, *J. Mater. Chem.* 3 (2015) 8865–8869.
- [49] B. Wang, S.M. Alhassan, S.T. Pantelides, *Phys. Rev. Appl.* 2 (2014) 1–7.
- [50] L. Wang, T. Zhang, S. Yang, F. Cheng, J. Liang, J. Chen, *J. Energy Chem.* 22 (2013) 72–77.
- [51] R.S. Assary, L.A. Curtiss, J.S. Moore, *J. Phys. Chem. C* 118 (2014) 11545–11558.
- [52] L.E. Camacho-Forero, T.W. Smith, S. Bertolini, P.B. Balbuena, *J. Phys. Chem. C* 119 (2015) 26828–26839.
- [53] J.J. Chen, R.M. Yuan, J.M. Feng, Q. Zhang, J.X. Huang, G. Fu, M. Sen Zheng, B. Ren, Q.F. Dong, *Chem. Mater.* 27 (2015) 2048–2055.
- [54] P. Canepa, S. Jayaraman, L. Cheng, N.N. Rajput, W.D. Richards, G.S. Gautam, L. A. Curtiss, K.A. Persson, G. Ceder, *Energy Environ. Sci.* 8 (2015) 3718–3730.
- [55] Q. Cheng, W. Xu, S. Qin, S. Das, T. Jin, A. Li, A.C. Li, B. Qie, P. Yao, H. Zhai, et al., *Angew. Chem. Int. Ed.* 58 (2019) 5557–5561.
- [56] Q. Wang, J. Zheng, E. Walter, H. Pan, D. Lv, P. Zuo, H. Chen, Z.D. Deng, B.Y. Liaw, X. Yu, et al., *J. Electrochem. Soc.* 162 (2015) A474–A478.
- [57] T. Gao, M. Noked, A.J. Pearce, E. Gillette, X. Fan, Y. Zhu, C. Luo, L. Suo, M. A. Schroeder, K. Xu, et al., *J. Am. Chem. Soc.* 137 (2015) 12388–12393.
- [58] B. Delley, *J. Chem. Phys.* 92 (1990) 508.

- [59] B. Delley, *J. Chem. Phys.* 113 (2000) 7756–7764.
- [60] J.P. Perdew, Y. Wang, *Phys. Rev. B* 45 (1992) 244–249.
- [61] J.P. Stewart, *MOPAC Manual*, seventh ed., 1993.
- [62] P.E. Blöchl, *Phys. Rev. B* 50 (1994) 17953–17979.
- [63] J.P. Perdew, K. Burke, M. Ernzerhof, *Phys. Rev. Lett.* 77 (1996) 3865–3868.
- [64] K. Leung, C.M. Tenney, *J. Phys. Chem. C* 117 (2013) 24224–24235.
- [65] A. Klamt, G. Schüürmann, *J. Chem. Soc., Perkin Trans. 2* (1993) 799–805.
- [66] M. Cossi, N. Rega, G. Scalmani, V. Barone, *J. Comput. Chem.* 24 (2003) 669–681.
- [67] S. Yanase, T. Oi, *J. Nucl. Sci. Technol.* 39 (2002) 1060–1064.
- [68] Y. Li, K. Leung, Y. Qi, *Acc. Chem. Res.* 49 (2016) 2363–2370.
- [69] I. Skarmoutsos, V. Ponnuchamy, V. Vetere, S. Mossa, *J. Phys. Chem. C* 119 (2015) 4502–4515.
- [70] M. Shakourian-Fard, G. Kamath, K. Smith, H. Xiong, S.K.R.S. Sankaranarayanan, *J. Phys. Chem. C* 119 (2015) 22747–22759.
- [71] B. Jiang, V. Ponnuchamy, Y. Shen, X. Yang, K. Yuan, V. Vetere, S. Mossa, I. Skarmoutsos, Y. Zhang, *J. Phys. Chem. Lett.* 7 (2016) 3554–3559.
- [72] A. Warshel, S.T. Russell, *Q. Rev. Biophys.* 17 (1984) 283–422.
- [73] D. Meyerstein, *Can. J. Chem.* 45 (1967) 884–886.
- [74] H. Sun, *J. Phys. Chem. B* 102 (1998) 7338–7364.
- [75] S. Nosé, *Mol. Phys.* 52 (1984) 255–268.
- [76] H.J.C. Berendsen, J.P.M. Postma, W.F. Van Gunsteren, A. Dinola, J.R. Haak, *J. Chem. Phys.* 81 (1984) 3684–3690.
- [77] I.A. Courtney, J.S. Tse, O. Mao, J. Hafner, J.R. Dahn, *Phys. Rev. B Condens. Matter* 58 (1998) 15583–15588.
- [78] M.I. Nandasiri, L.E. Camacho-Forero, A.M. Schwarz, V. Shutthanandan, S. Thevuthasan, P.B. Balbuena, K.T. Mueller, V. Murugesan, *Chem. Mater.* 29 (2017) 4728–4737.
- [79] Z. Liu, S. Bertolini, P.B. Balbuena, P.P. Mukherjee, *ACS Appl. Mater. Interfaces* 8 (2016) 4700–4708.
- [80] F. He, X. Wu, J. Qian, Y. Cao, H. Yang, X. Ai, D. Xia, *J. Mater. Chem. A* 6 (2018) 23396–23407.
- [81] N. Kang, Y. Lin, L. Yang, D. Lu, J. Xiao, Y. Qi, M. Cai, *Nat. Commun.* 10 (2019) 4597.
- [82] W.-J. Zhang, *J. Power Sources* 196 (2011) 13–24.
- [83] S. Homaeigohar, M. Elbahri, *NPG Asia Mater.* 9 (2017) e427.
- [84] J. Zheng, M. Gu, M.J. Wagner, K.A. Hays, X. Li, P. Zuo, C. Wang, J. Zhang, L. Liu, J. Xiao, *J. Electrochem. Soc.* 160 (2013) 1624–1628.
- [85] L. Cheng, L.A. Curtiss, K.R. Zavadil, A.A. Gewirth, Y. Shao, K.G. Gallagher, *ACS Energy Lett.* 1 (2016) 503–509.
- [86] O. Borodin, L. Suo, M. Gobet, X. Ren, F. Wang, A. Faraone, J. Peng, M. Olguin, M. Schroeder, M.S. Ding, et al., *ACS Nano* 11 (2017) 10462–10471.